Structural, elastic, and vibrational properties of phase H: A first-principles simulation*

Chao-Jia Lv(吕超甲)[1], Lei Liu(刘雷)[1,2,†], Yang Gao(高阳)[3], Hong Liu(刘红)[1], Li Yi(易丽)[1], Chun-Qiang Zhuang(庄春强)[4], Ying Li (李营)[1,2], and Jian-Guo Du(杜建国)[1]

[1] *Key Laboratory of Earthquake Prediction, Institute of Earthquake Science, China Earthquake Administration, Beijing* 100036, *China*
[2] *National Key Laboratory of Shock Wave and Detonation Physics, Mianyang* 621000, *China*
[3] *Department of Mechanical Engineering, Texas Tech University, Lubbock* 79409, *USA*
[4] *Institute of Microstructure and Properties of Advanced Materials, Beijing University of Technology, Beijing* 100124, *China*

(Received 8 October 2016; revised manuscript received 2 March 2017; published online 20 April 2017)

Phase H ($MgSiO_4H_2$), one of the dense hydrous magnesium silicates (DHMSs), is supposed to be vital to transporting water into the lower mantle. Here the crystal structure, elasticity and Raman vibrational properties of the two possible structures of phase H with *Pm* and $P2/m$ symmetry under high pressures are evaluated by first-principles simulations. The cell parameters, elastic and Raman vibrational properties of the *Pm* symmetry become the same as the $P2/m$ symmetry at ~ 30 GPa. The symmetrization of hydrogen bonds of the *Pm* symmetry at ~ 30 GPa results in this structural transformation from *Pm* to $P2/m$. Seismic wave velocities of phase H are calculated in a range from 0 GPa to 100 GPa and the results testify the existence and stability of phase H in the lower mantle. The azimuthal anisotropies for phase H are $A_{P0} = 14.7\%$, $A_{S0} = 21.2\%$ ($P2/m$ symmetry) and $A_{P0} = 16.4\%$, $A_{S0} = 27.1\%$ (*Pm* symmetry) at 0 GPa, and increase to $A_{P30} = 17.9\%$, $A_{S30} = 40.0\%$ ($P2/m$ symmetry) and $A_{P30} = 19.2\%$, $A_{S30} = 37.8\%$ (*Pm* symmetry) at 30 GPa. The maximum V_P direction for phase H is [101] and the minimum direction is [110]. The anisotropic results of seismic wave velocities imply that phase H might be a source of seismic anisotropy in the lower mantle. Furthermore, Raman vibrational modes are analyzed to figure out the effect of symmetrization of hydrogen bonds on Raman vibrational pattern and the dependence of Raman spectrum on pressure. Our results may lead to an in-depth understanding of the stability of phase H in the mantle.

Keywords: phase H, elastic properties, Raman properties, first principles

PACS: 74.25.nd, 62.50.–p, 63.20.dk **DOI:** 10.1088/1674-1056/26/6/067401

1. Introduction

The presence of water in the lower mantle has various functions, such as dramatically lowering the melting temperature of mantle rocks, causing arc magmatism, reducing the magma viscosity and density, enhancing magma migration, influencing the elastic and rheological properties of the mantle, and broadening seismic discontinuities.[1] It is now accepted that water can percolate through the Earth's interior by subducting slabs through hydrous minerals, such as serpentine.[2,3] The serpentine can transform into several dense hydrous magnesium silicates (DHMSs), depending on the pressure and temperature conditions.[4–6] Since the first discovery of 10-Å phase,[7] dense hydrous magnesium silicates including 3.65-Å phase, phase A, phase B, superhydrous phase B, phase D, phase E, etc. have received considerable attention because of their presumed role in the water resources of the Earth.[8–10]

Phase D ($MgSi_2O_6H_2$) has been considered to be the most thermodynamically stable phase under lower mantle conditions.[11,12] It has been discovered that phase D transforms into the phase H at 44 GPa.[13] Phase H was first announced to be stable up to 52 GPa and had a crystal structure similar to that of $CaCl_2$-type SiO_2, of which half of the Si atoms replace Mg atoms and hydrogen atoms are located at the edges of the vacant octahedral sites (Fig. 1). Early theoretical studies predicted the crystal structure of phase H to be monoclinic with $P2/m$ symmetry.[14] Since then, phase H has been discussed to evaluate its structural stability, elastic properties and the possibility of forming a solid solution with δ-AlOOH in the lower mantle condition.[14–16] Yet, due to the fact that different analytical methods are adopted, the results of previous studies are controversial. Possible structure of phase H suggested by Bindi *et al.*[15] was based on energy-dispersive x-ray diffraction while that by Nishi *et al.*[16] was based on in situ single-crystal x-ray diffraction. Besides, the quality of diffraction data was not accurate enough to determine the positions of hydrogen atoms. On the other hand, the work provided by first principles calculations could not take the thermal vibration effect into consideration.[17] As a result, the structure parameters and symmetry of phase H are discrepant in different studies.

*Project supported by the Key Laboratory of Earthquake Prediction, Institute of Earthquake Science, China Earthquake Administration (CEA) (Grant Nos. 2016IES010104 and 2012ES0408) and the National Natural Science Foundation of China (Grant Nos. 41174071, 41273073, 41373060, and 41573121).

†Corresponding author. E-mail: liulei@cea-ies.ac.cn

© 2017 Chinese Physical Society and IOP Publishing Ltd

In this study, in order to further understand the stability of phase H under high pressure, the crystal structure, elastic constants, seismic velocities and anisotropies of the two different possible symmetry phase H's (*Pm* and $P2/m$ symmetry) are calculated by using first-principles simulations. The $P2/m$ symmetry is based on the fully optimized structure by Tsuchiya and Mookherjee[17] while Pm symmetry possesses hydrogen atoms drawn at the Wyckoff position, which is inspired by previous single-crystal x-ray diffraction research.[16] Raman vibrational properties are also analyzed to evaluate the changes of the crystal structure with pressure.

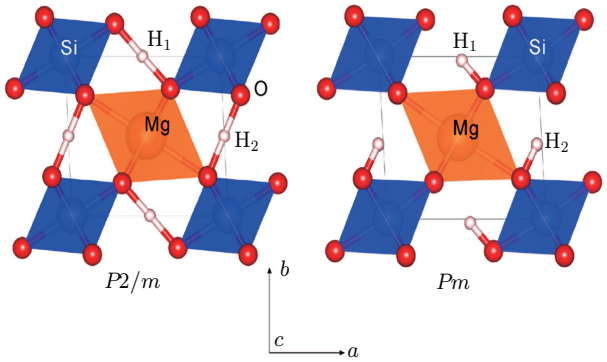


Fig. 1. (color online) Structures of phase H with $P2/m$ and *Pm* symmetry. The hydrogen atoms are not located in the middle of two oxygen atoms in structure with *Pm* symmetry (right), however, hydrogen atoms in $P2/m$ structure (left) are located on the right side in the middle of couples of oxygen atoms.

2. Methods

2.1. Computational methods

The first-principles calculations were performed using density functional perturbation theory (DFPT),[18] density functional theory (DFT),[19,20] and the plane wave pseudopotential method, as implemented in the CASTEP codes.[21] The generalized gradient approximation (GGA) with PBE parameterization was adopted to describe the exchange-correlation functional.[22] GGA functional was tested to provide a better performance than local density approximation (LDA) for simulations of hydrogen bonding.[23,24] Norm-conserving pseudopotentials[25] were employed to model the electron–ion interaction. The electronic wave functions were expanded in plane-waves with a kinetic energy cutoff of 1200 eV. The irreducible Brillouin zone of the phase H is sampled on a $5\times8\times5$ Monkhorst–Pack mesh.[26] Both energy cutoff and *k*-point mesh are selected after a series of convergence tests for the precision of the calculation. The tests show that the difference among lattice parameters and total energy are restrained under 0.01% at higher accuracy. The total energy convergence criterion of 5×10^{-7} a.u. was used in the self-consistent field calculations.

The structures of phase H used in this study possess monoclinic structures with $P2/m$ and *Pm* symmetries which were proved to be more thermodynamically stable[14] (Fig. 1). These two adopted structures have ordered Mg and Si arrangements which are essential for the calculation of polarizability and Raman spectra. However, the structures of synthetic experimental samples belong to orthorhombic structures with symmetry *Pnnm*[15] or with $P2_1nm$.[16] The difference from our calculation was that the structures found in experiments have disordered sequences of Mg and Si atoms in which the occupancy of Mg and Si for each center of the octahedron were both 50%. All structure parameters and atomic coordinates were fully relaxed to a static configuration (0 K) by using BFGS geometry optimization algorithm.[27] The elastic constants were determined by stress–strain relationships.[28] The magnitude of all applied strains was 0.003 and the linear relationship was ensured to be enough for this strain range. The Raman properties were calculated using the linear response density functional perturbation theory (DFTP).[29] Spatial derivatives of the macroscopic polarization were calculated numerically along the eigenvectors of each Raman active phonon mode by calculating the polarization for each displacement through using the linear response formalism.[30] Once these derivatives are known, the Raman cross-section through an appropriate averaging space can be calculated. More information about Raman spectra by density functional theory was listed by Porezag and Pederson[31] and Refson *et al.*[32]

2.2. Benchmark calculations

To assess the performances of the DFT and DFPT total-energy approach in our study, test calculations of the cell parameters and elastic constants of phase H were performed. The differences in cell volumes, lengths of *a*, *b*, and *c* axes between the calculated results and corresponding experimental values[16] are 0.1%, 1.2%, 0.7%, and 0.4% respectively, or 2.7%, 1.7%, 0.6%, and 0.7% compared with the other experimental results[15] (Table 1). Comparing our calculated results with the calculated results of Tsuchiya,[14] the tiny differences can be ignored. Since no experimental results of elastic constants are available, the calculated values of elastic constants[17] are adopted for comparison. The differences in C_{11}, C_{22}, C_{33}, C_{44}, C_{55}, C_{66}, C_{12}, and C_{13} between this work and previous study are 2.2%, 5.4%, 2.9%, 6.6%, 3.2%, 10.4%, 2.8%, and 6.7% at 30 GPa, respectively. Notably, the pseudopotential of magnesium in former research[17] is generated by the method of von Barth and Car. In contrast, here we adopted norm-conserving pseudopotentials for all atoms, which may lead to the discrepancies in elastic constants. Such close agreement between the experimental and calculated values of lattice parameters and elastic constants demonstrates the validity of this computational project.

Table 1. Benchmark calculations results.

P/GPa	a/Å	b/Å	c/Å	γ/(°)	V/Å^3	R_{O-H}/Å	$R_{O\cdots O}$/Å	Symmetry	Reference
0	4.813	4.350	2.863	93.35	59.84	1.035	2.555	Pm	this work
0	4.733	4.325	2.842	90	58.18	1.010	2.460	$Pnnm$	[15]
0	4.786	4.328	2.848	93.30	58.90	1.039	2.580	$P2/m$	[17]
42	4.532	4.061	2.689	91.35	49.48	1.174	2.347	$P2/m$	this work
42	4.478	4.091	2.700	90	49.46	–	–	$P2_1nm$	[16]

3. Results

3.1. Crystal structure

Ever since the first-principles prediction of this new mineral was proposed,[14] phase H has been observed in the two separate experimental research studies.[15,16] However, due to the difficulties in detecting the positions of hydrogen atoms and pressure-induced rapid amorphization of the sample,[15,16] the structure of phase H was roughly judged to be an orthorhombic system with symmetry $P2_1nm$ (δ-AlOOH-type structure) and orthorhombic system with symmetry $Pnnm$ ($CaCl_2$ type structure), respectively. However, theoretical studies proposed different crystal structures: monoclinic structures with Pm and $P2/m$ symmetry, which have been proved to be more thermodynamically stable than the experimental ones. The major difference between the theoretical and experimental structures is the arrangement of Mg and Si atoms. Both experimental structures possess disordered distributions of cations (Mg, Si), while theoretical structures possess ordered distributions of Mg and Si in octahedral sites. Furthermore, the $P2/m$ symmetry possesses symmetric hydrogen bonds, while the Pm symmetry possesses asymmetric hydrogen bonds. The Pm and $P2/m$ symmetries slightly deviate from experiential structures and were provided to be precise enough for the simulation of phase H.[17] Therefore, we select the two structures from theoretical studies as our investigation objects.[14]

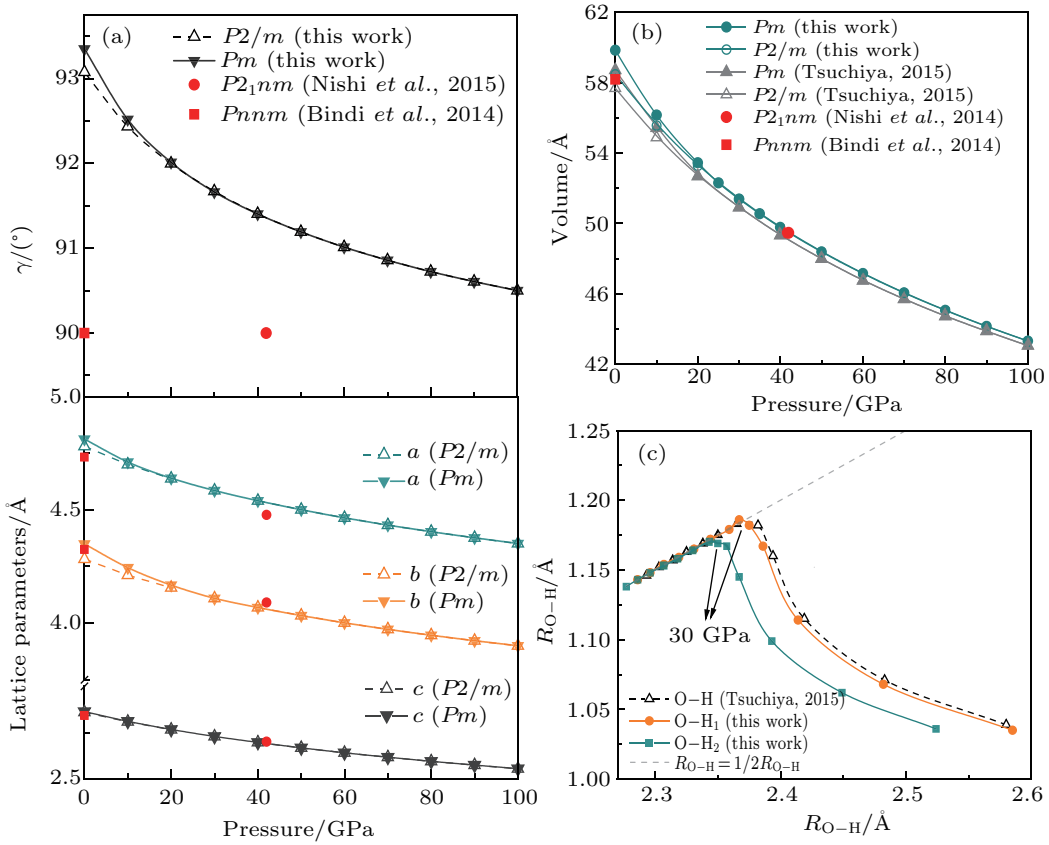


Fig. 2. (color online) Lattice parameters of phase H each as a function of pressure: (a) γ angle and a, b, and c axes of phase H, (b) cell volume of phase H, (c) symmetrization of hydrogen bonds in phase H with Pm symmetry. The black dashed line represents the function of $R_{O-H} = 0.5 \times R_{O\cdots O}$. At about 30 GPa, R_{O-H1} and R_{O-H2} reach the half of $R_{O\cdots O}$.

Geometry optimization has been conducted on both Pm and $P2/m$ structures from 0 GPa to 100 GPa. The detailed cell parameters of the two structures are listed in Table 2 and Supplement Tables A1, A2, and A3 in Appendix A. Figure 2 shows the pressure-lattice parameters of the two structures under high pressures. The lengths of a, b, and c axes decrease at almost the same ratio with increasing pressure, at the same time the γ angle decreases to 90°. Two-stage

changes of lattice parameters of the two structures with increasing pressure are observed. The variation tendencies for lattice parameters of the two structures approach each other from 0 GPa to 30 GPa, above which the two structures almost keep the same lattice parameters. A possible explanation to this result is the symmetrization of hydrogen bonds. Since the first prediction of symmetrization of the hydrogen bonds in ice VII,[33] a large number of research studies have been conducted to understand the pressure dependence of hydrogen bonds' symmetrization.[34–36] It is widely accepted that the bonded O–H distance shows relevance to the O···O distance in many O–H···O geometry systems. In a weak hydrogen bond system with phase H, where O···O distance is more than 2.6 Å, the hydrogen bond length is almost fixed at 1 Å. Once the O···O bond is under high pressure, the O···O distance would decrease to around 2.4 Å and the O–H length could increase to the half of the O···O distance, where the hydrogen is located in the middle of two oxygen atoms. The hydrogen bonds of phase H with *Pm* symmetry become symmetrized at pressures higher than 30 GPa (Fig. 2). When the O···O distance reduces with pressure increasing from 0 GPa to 30 GPa, the length of O–H bond also increases rather than falls. The length of O–H is kept at half of the distance of O···O under higher pressures, which means that the hydrogen atom is located in the middle of the pair of oxygen atoms. This result indicates that phase H would turn from *Pm* structure with asymmetric hydrogen bonds into the $P2/m$ structure with symmetric hydrogen bonds at about 30 GPa. It is also the reason that the two structures with different initial lattice parameters can become the same at pressures higher than 30 GPa.

The volume–pressure relationships (Fig. 2) for the two structures of phase H are well described by the finite strain formulation of the third order Birch–Murnaghan.[37] Values of bulk moduli (K_0) are 156.2 GPa and 177.9 GPa, values of the pressure derivative of the zero pressure bulk modulus (K_0') are 4.40 and 4.18 and the values of initial unit-cell volume (V_0) are 59.3 Å^3 and 58.4 Å^3 for *Pm* and $P2/m$ structures, respectively. The differences in initial unit-cell volume, K_0 and V_0, between the results in this work (*Pm*) and previous calculation results $(P2/m)$[17] are 2.9%, 5.9%, and 1.6%, respectively.

Table 2. Structural properties of phase H.

Parameter	*Pm* at 0 GPa	$P2/m$ at 0 GPa	*Pm* at 30 GPa	$P2/m$ at 30 GPa
a/Å	4.812	4.780	4.585	4.585
b/Å	4.349	4.282	4.109	4.109
c/Å	2.863	2.859	2.728	2.728
γ/(°)	93.349	93.076	91.663	91.671
V/Å^3	59.838	58.467	51.382	51.379
ρ/(g/cm^3)	3.286	3.363	3.826	3.827
Hydrogen bonds	asymmetric	symmetric	symmetric	symmetric
O···O (H_1)	2.585	2.440	2.375	2.376
O–H (H_1)	1.035	1.220	1.193	1.188
O···O (H_2)	2.524	2.408	2.357	2.356
O–H (H_2)	1.036	1.204	1.167	1.178
V_{MgO6}/Å^3	8.210	8.143	7.390	7.389
V_{SiO6}/Å^3	12.377	12.257	10.376	10.375
K_0/GPa	156.24	177.90		
K'	4.46	4.18		
V_0/Å^3	59.32	58.45		

Notes: H_1 lies in the plane of Si atoms along the [001] direction while H_2 is located in the plane of Mg atoms.

3.2. Elasticity

The pressure-dependent elastic constants for the two phase H are shown in Fig. 3 and Supplement Table A3. All elastic constants, except for C_{15} and C_{25} both of which maintain around 0 GPa, increase with pressure rising, which is different from the previous result.[17] We think that the discrepancy of pseudopotential selected for magnesium might result in the differences in lattice parameters. The differences in lattice parameters in turn result in the discrepancies in elastic constants. For instance, the values of lattice parameter a in this work and the previous work[17] have a difference of 0.40% under 30 GPa, and this leads to a difference of 0.58% in elastic constant C_{11}. The principle elastic constants C_{11} and C_{22}, the shear elastic constant C_{66}, and the off-diagonal elastic constants C_{12}, C_{23}, and C_{46} for *Pm* symmetry are significantly smaller than those of the $P2/m$ symmetry under low pressures. These constants also sharply rise from 25 GPa to 30 GPa, which is also the pressure range of symmetrization of hydrogen bonds. These results indicate that the elastic constants of *Pm* symmetry are obviously dependent on the strength of the hydrogen bond. Namely, the symmetrization of hydrogen bonds increases the stiffness of phase H in the direction perpendicular to the c axis direction. Similar anomalous phenomena have been reported in phase D and δ-AlOOH.[35,36] Above 30 GPa, elastic constants for the two structures become equal to each other.

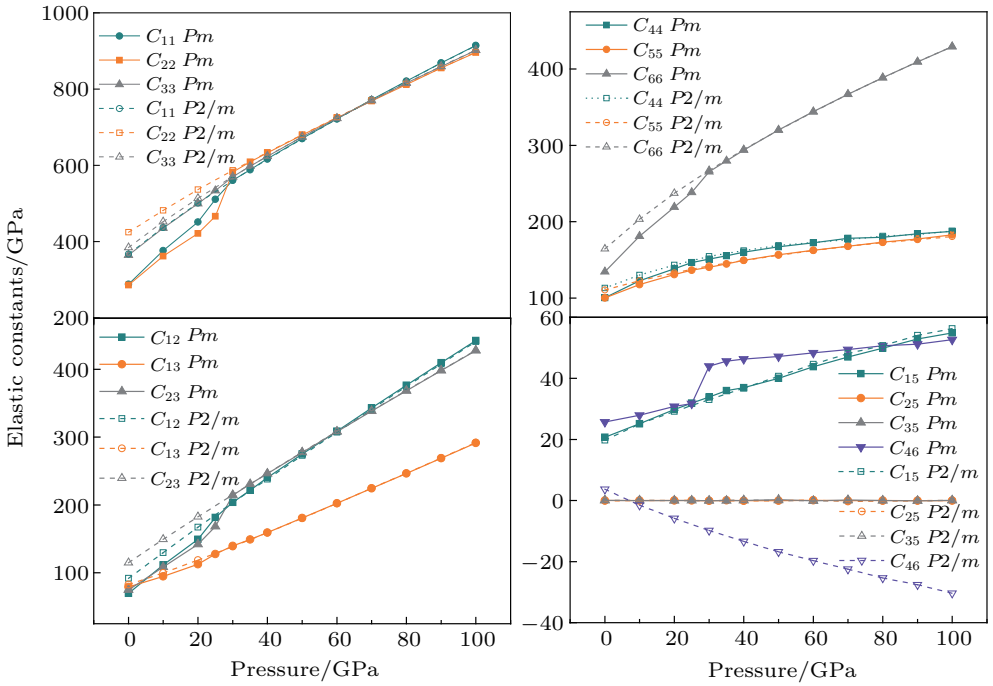


Fig. 3. (color online) Pressure-dependent elastic constants for phase H.

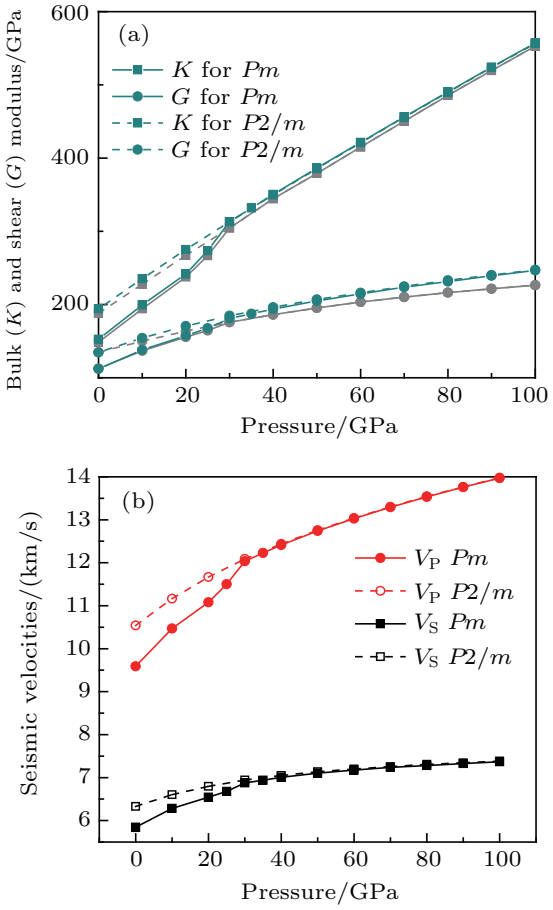


Fig. 4. (color online) Bulk and shear moduli (a) and seismic velocities (b) of phase H as a function of pressure. Grey lines and points in panel (a) stand for K and G from Ref. [17].

Bulk (K) and shear (G) moduli are determined by the Voigt–Reuss–Hill average (Fig. 4). The bulk and shear moduli of phase H with Pm symmetry show anomalous increases at 25 GPa–30 GPa. The anomalous pressure-dependent bulk and shear moduli are also related to the symmetrization of hydrogen bonds. The bulk modulus K_0 of phase H with Pm symmetry is about 27% smaller than that of $P2/m$ symmetry. Under higher pressures (>30 GPa) the bulk and shear moduli of these two structures are almost the same.

Sound wave velocities from seismic observation can reflect the composition and structure of the mantle. For crystalline material, the compressional wave velocity (V_P) and shear wave velocity (V_S) are related to the bulk and shear moduli via

$$V_P = \sqrt{\left(K + \left(\frac{3}{4}\right)G\right)/\rho},$$
$$V_S = \sqrt{G/\rho},$$

where ρ is the mass density determined by the equilibrium of crystal lattice from the first-principles optimization, K is the bulk modulus, and G is the shear modulus. The V_P and V_S of phase H with $P2/m$ symmetry increase smoothly with increasing pressure. The V_P and V_S of Pm symmetry sharply increase from 25 GPa to 30 GPa (Fig. 4) compared with those of $P2/m$. The pressure dependent V_P and V_S of phase H with Pm and $P2/m$ symmetry show similar tendencies to those of K and G. At pressures above 30 GPa, the values of V_P and V_S of Pm and $P2/m$ symmetry are almost identical. The symmetrization of hydrogen bonds also generally takes place in plenty of minerals under high pressures, such as ice, δ-AlOOH and hydrous silica.[36,38] Therefore, the symmetrization of hydrogen bonds in dense hydrous silicate may contribute to the abnormally pressure-dependent V_P and V_S in the upper mantle. The

$P2/m$ symmetry shows higher density and velocity than the Pm symmetry under pressure lower than 30 GPa. The transition from Pm to $P2/m$ may somewhat contribute to the leaps of density and seismic wave velocity in the transition layer of the mantle.

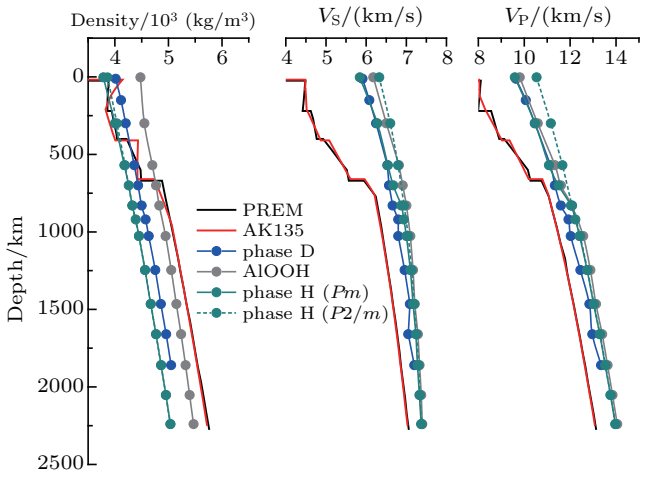


Fig. 5. (color online) Densities and seismic wave velocities of phase H, phase D and δ-AlOOH. Data for phase D are cited from Ref. [49] while data for AlOOH are taken from Ref. [50].

The values of density, V_P and V_S of phase D, H, and δ-AlOOH under high pressures are plotted in Fig. 5. Phase D shows the minimal density and velocities while δ-AlOOH possesses the maximal density and velocities in the hull depth range. It has been proved that phase D would transform into phase H at pressures ranging from about 40 GPa to 50 GPa, and phase H is inclined to form solid solutions with δ-AlOOH while δ-AlOOH and H show similar structures.[15,16,39] The transformation process from phase D to phase H and finally to solid solution of phase H and δ-AlOOH results in the increasing of density and velocities, which show the consistent trends with PREM and AK135 patterns. δ-AlOOH is believed to be stable under lower mantle condition. The forming of solid solution with phase H implicates that the water may have an opportunity to be carried to the lower region of the mantle and even the border of the mantle and core of the Earth. Ultimately, water should be released freely after the solid solution of δ-AlOOH and phase H have been heated up by the core, which may contribute to the phenomena of ultralow-velocity regions[40] and large low-shear-velocity provinces[41] detected in the underpart of the mantle.

Single crystal seismic velocities for phase H are also calculated by solving Cristoffel's equation:[42] $\det|c_{ijkl}n_jn_l - PV^2\delta_{ij}| = 0$, where n, ρ, V, and δ_{ij} are the propagation direction, density, elastic wave velocity, and Kronecker delta, respectively. Longitudinally and two orthogonally polarized shear wave velocities of the Pm and $P2/m$ structure at 0, 30, and 60 GPa are shown in Fig. 6 by using the MSAT codes.[43] At 0 GPa, both V_P and V_S of Pm structure (solid lines) are significantly smaller than those of $P2/m$ structure (dashed lines) except for those in the [001] direction, since there are only octahedrons of Si and O but no hydrogen bonds parallel to [001] direction. With the symmetrization of hydrogen bonds at 30 GPa, the patterns of single crystal seismic velocities for the two structures become similar. As pressure increases, the difference in anisotropy of seismic velocity between the two structures decreases significantly. The anisotropic properties of phase H at 30 GPa and 60 GPa are almost the same, so the primary reason why the anisotropy changes is crystal structural rearrangement (symmetrization of hydrogen bonds). The maximal V_P direction for phase H is [101] and the minimal direction is [110]. Azimuthal anisotropy for P and S waves is defined as $A = (V_{max} - V_{min})/V \times 100$, where V_{max} and V_{min} are the maximal and minimal velocity, respectively. The azimuthal anisotropies for phase H are $A_{P0} = 14.7\%$, $A_{S0} = 21.2\%$ ($P2/m$ symmetry) and $A_{P0} = 16.4\%$, $A_{S0} = 27.1\%$ (Pm symmetry) at 0 GPa, and increase to $A_{P30} = 17.9\%$, $A_{S30} = 40.0\%$ ($P2/m$ symmetry) and $A_{P30} = 19.2\%$, $A_{S30} = 37.8\%$ (Pm symmetry) at 30 GPa. Those results show that the phase H can be a significant source of anisotropy in the lower mantle.

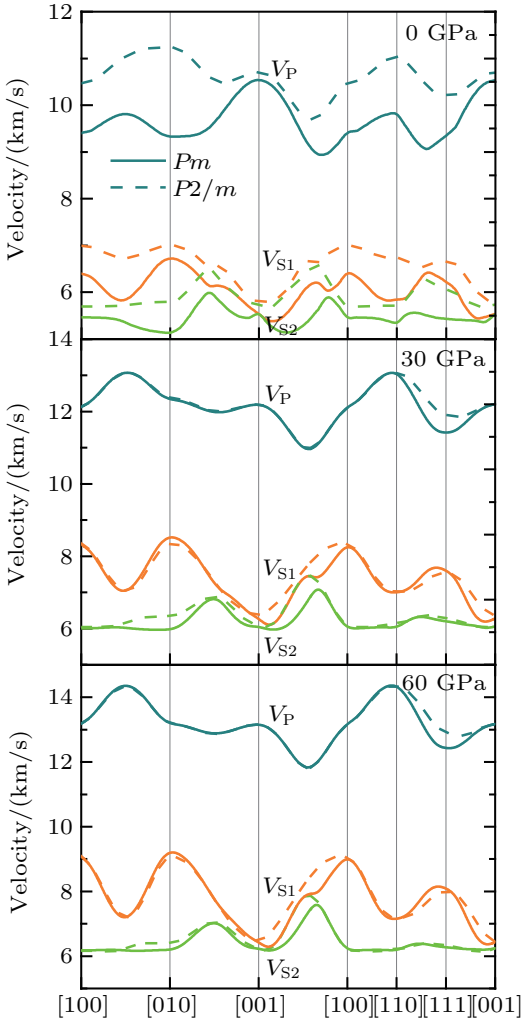


Fig. 6. (color online) Single crystal seismic velocities of phase H under 0, 30, and 60 GPa.

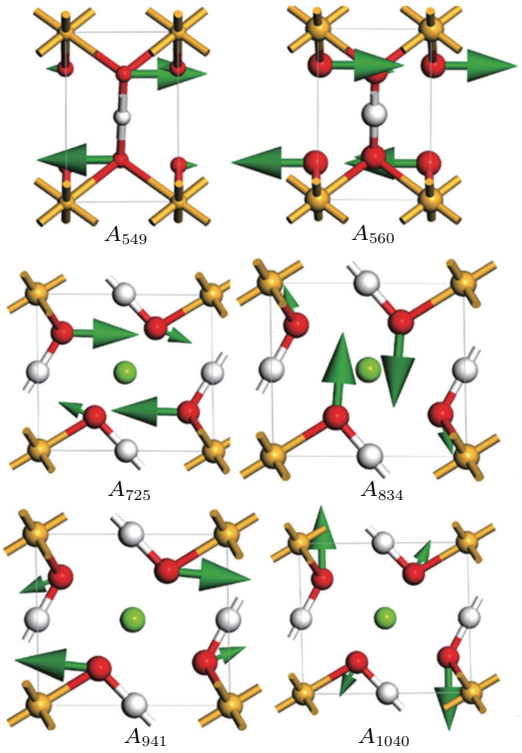


Fig. 7. (color online) Vibrational patterns of the $P2/m$ structure under 0 GPa. Yellow, green, red, and white balls donate Si, Mg, O, and H atoms, respectively. The direction and scale of arrow indicate vibrational orientation and relative vibrational intensity.

3.3. Vibration

Vibrational spectra of crystalline solids can be interpreted by using the factor group analysis.[44] For phase H with $P2/m$ symmetry, the irreducible representation of optical vibrations is $\Gamma_{\text{OPTIC}} = 4\text{Ag} + 5\text{Au} + 2\text{Bg} + 10\text{Bu}$. Since the structure is centro-symmetric, IR and Raman-active modes are mutually exclusive.[45] The Raman-active modes are $\Gamma_{\text{Raman}} = 4\text{Ag} + 2\text{Bg}$. As for Pm structure, the optical vibration mode is $\Gamma_{\text{OPTIC}} = 14A' + 7A''$ and Raman-active mode is $\Gamma_{\text{Raman}} = 14A' + 7A''$. The Raman-active modes for experimental results ($Pnnm$ and $P21nm$) are $3A_g + 3B_{1g} + 3B_{2g} + 3B_{3g}$ and $3A_1 + 3A_2 + 3B_1 + 3B_2$, which deviate from calculated ones since different symmetries are involved. Nevertheless, the variance is quite acceptable as the major difference between experimental and calculated structures is the γ angle which distorts within a range of 3 degrees.

Raman frequencies of the two phase H structures are calculated and plotted each as a function of pressure in Fig. 8. The number of active Raman modes for $P2/m$ symmetry remains constant in a pressure range from 0 GPa to 100 GPa. In addition, the vibrational frequencies increase with the augment of pressure, which is normal behavior resulting from the increased repulsion between neighbor atoms.[46] The intensities of all Raman-active modes except for A_{560} decrease under pressure (Supplement Tables A4, A5, and A6 in Appendix A). As for $P2/m$ symmetry, all Raman modes (Fig. 7) are only related to the motion of oxygen atoms. No contributions from the motions of Mg, Si, and H atoms are detected. The A_{549} and A_{560} modes only have atomic vibrations parallel to the c axis, and the A_{725}, A_{834}, A_{941}, and A_{1040} modes only have atomic vibrations perpendicular to the c axis. Raman intensities for vibrations parallel to c axis (A_{549} and A_{560}) are smaller than those of vibrations perpendicular to c axis (A_{725}, A_{834}, A_{941}, and A_{1040} modes) (Supplement Table A4 in Appendix A). The results suggest that the Raman vibration in phase H with symmetric hydrogen bonds is mainly controlled by displacements of oxygen atoms parallel to (001) plane.

At 0 GPa, 21 Raman modes are observed in phase H with Pm symmetry. These modes can be classified as two groups. Group 1 includes 15 vibrational modes with frequencies ranging from 226 cm^{-1} to 780 cm^{-1}. The rest of these modes with frequencies in a range from 1009 cm^{-1} to 2470 cm^{-1} belong to group 2. Distortions and relative displacements of Si (or Mg) and O are observed in group 1 while only displacement of H, stretching and bending of hydrogen bonds are observed in group 2. The O–H stretching modes (A_{2452} and A_{2479}) have the maximal intensities, because of the long-range electrostatic interactions between O–H groups.[41]

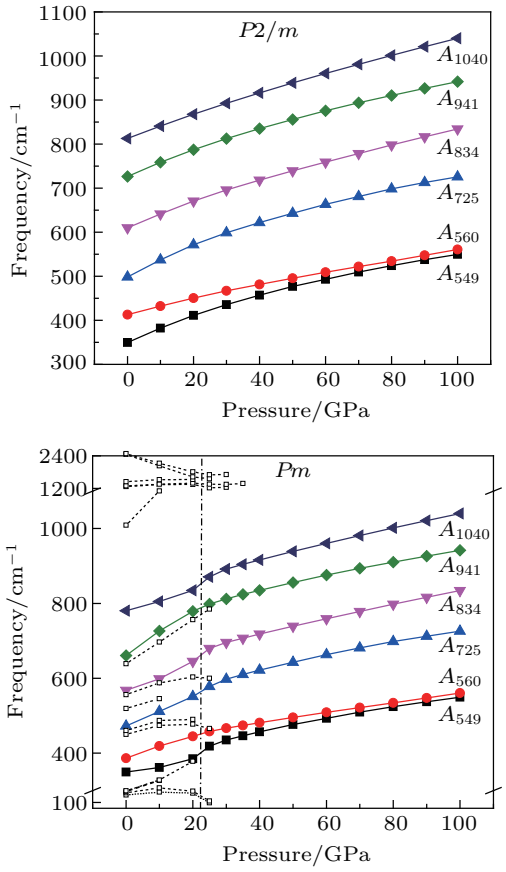


Fig. 8. (color online) Plots of Raman-active frequency of phase H versus pressure. Dasheed plots and lines refer to the Raman modes which are inactive under high pressures.

The vibrational patterns of Pm symmetry can be divided into two stages: from 0 GPa to 30 GPa and from 30 GPa to 100 GPa (Fig. 8), according to the symmetrization of hydro-

gen bonds at about 30 GPa. All the vibrational modes belonging to group 2 (in a frequency range from 1009 cm^{-1} to 2479 cm^{-1}) disappear at pressures higher than 30 GPa. The reason is that the reduction of O···O distances and the symmetrization of hydrogen bonds restrict the ability for hydrogen atoms to motion.[47] Besides, 8 vibrational modes in group 1 which relate to the motions of Mg or Si atoms vanish before being pressurized to 30 GPa. Finally, in the *Pm* symmetry there are only 6 vibration modes (A_{549}, A_{560}, A_{725}, A_{834}, A_{941}, and A_{1040}) that remain Raman-active, the number of which modes (i.e., 6) is exactly the number of vibration modes that are Raman active in the $P2/m$ symmetry. Despite the obvious differences between Raman spectra at 0 GPa, the Raman frequencies and intensities for *Pm* and $P2/m$ symmetry are quite alike at pressures higher than 30 GPa (Supplement Tables A4, A5, and A6 in Appendix A).

Six Raman modes: A_{549}, A_{560}, A_{725}, A_{834}, A_{941}, and A_{1040} of *Pm* symmetry are taken into account for calculating the pressure derivatives ($\mathrm{d}v_i/\mathrm{d}P$) in a pressure range from 0 GPa to 100 GPa because the remaining modes vanish under high pressures (> 30 GPa) (Table 1). The pressure derivatives of all modes for phase H are positive, which implies the strengthening of the structure.[48] Unlike the Raman shift frequency of $P2/m$ symmetry which is linearly dependent on pressure, the pressure derivatives of *Pm* symmetry can be classified as 2 groups. At low pressures (< 25 GPa), the pressure derivatives of Raman frequencies for *Pm* symmetry are larger than those for $P2/m$ symmetry. Also, the derivatives for both structures become similar at high pressures (> 30 GPa). A conspicuous jump of frequencies for *Pm* structure takes place at pressures between 25 GPa to 30 GPa, which corresponds to symmetrization of hydrogen bonds.

Table 3. Pressure shifts of the Raman modes of phase H.

Symmetry	Mode/cm^{-1}	$(\mathrm{d}v_i/\mathrm{d}P)/(cm^{-1}/GPa)$		
		$P2/m$	*Pm* (0–20 GPa)	*Pm* (25–100 GPa)
Bg	549	1.95	1.78	1.71
Bg	560	1.44	2.91	1.35
Ag	725	2.2	3.95	1.93
Ag	834	2.19	3.87	2.02
Ag	941	2.11	5.9	1.9
Ag	1040	2.25	2.73	2.18

4. Conclusions and perspectives

The phase H ($MgSiO_4H_2$), as an important candidate for transporting water into the deep Earth, is stable at pressures greater than the stability field of phase D, and separately discussed to evaluate its structure stability, elastic properties and the possibility of forming a solid solution with δ-AlOOH in the lower mantle condition.[14–16] In order to understand the stability of phase H under high pressure, first-principles simulations are carried out to investigate the structural, elastic, and vibrational properties of phase H with the two possible symmetric structures: *Pm* and $P2/m$. The results indicate that the two structures show similar structural parameters, elastic and vibrational properties at pressures higher than 30 GPa. The reason is the symmetrization of hydrogen bonds. The symmetrization of hydrogen bonds also generally takes place in plenty of minerals under high pressure, such as ice, δ-AlOOH and hydrous silica.[36,38]

The V_P and V_S of phase H with *Pm* symmetry sharply increase from 25 GPa to 30 GPa compared with those with $P2/m$ symmetry, and when pressure is larger than 30 GPa, the values of V_P and V_S of *Pm* and $P2/m$ symmetry are almost identical. In other words, the symmetrization of hydrogen bonds made the seismic velocities of phase H increase. Therefore, the symmetrization of hydrogen bonds in dense hydrous silicate may lead to the abnormal pressure dependence of V_P and V_S and the formation of a high-velocity layer in the mantle. The azimuthal anisotropies for phase H are $A_{P0} = 14.7\%$, $A_{S0} = 21.2\%$ ($P2/m$) and $A_{P0} = 16.4\%$, $A_{S0} = 27.1\%$ (*Pm*) at 0 GPa, and increase to $A_{P30} = 17.9\%$, $A_{S30} = 40.0\%$ ($P2/m$ symmetry) and $A_{P30} = 19.2\%$, $A_{S30} = 37.8\%$ (*Pm* symmetry) at 30 GPa. So phase H might be one of the sources of the velocity anomalies and anisotropy in the upper part of the lower mantle. Compared with phase D and δ-AlOOH, phase H shows small density but fast seismic velocity, which might contribute to the anomalous phenomenon of seismic velocity in the lower mantle.

Raman spectra of phase H show the effects of symmetrization of hydrogen bonds on vibrational frequency and intensity. At 0 GPa, 21 Raman modes are observed in phase H with *Pm* symmetry. As for $P2/m$ symmetry, 6 Raman modes are observed at 0 GPa. However, only 6 Raman modes in each phase H with *Pm*-to-$P2/m$ symmetry are detected under higher pressure (> 30 GPa). When pressure is higher than 30 GPa, Raman frequencies of *Pm* symmetry are the same as those of $P2/m$ symmetry, which indicates the transformation from *Pm* to $P2/m$ symmetry as a result of symmetrization of hydrogen bonds. The values of pressure derivative ($\mathrm{d}v_i/\mathrm{d}P$) of all Raman modes are positive. All these results conduce to the understanding of the stability of phase H in the mantle.

Appendix A: Supplementary tables

Some structure parameters for *Pm* and $P2/m$ structures under pressure are listed in the following tables.

Table A1. Structure parameters for $P2/m$ structure under pressures.

P/GPa	0	10	20	30	40	50	60	70	80	90	100
a/Å	4.78	4.70	4.64	4.59	4.54	4.50	4.46	4.43	4.40	4.37	4.35
b/Å	4.28	4.21	4.16	4.11	4.07	4.03	4.00	3.97	3.95	3.92	3.90
c/Å	2.86	2.81	2.77	2.73	2.70	2.67	2.64	2.62	2.59	2.57	2.55
β/(°)	93.08	92.44	92.00	91.67	91.40	91.19	91.01	90.86	90.72	90.60	90.51
V/Å^3	58.47	55.56	53.27	51.38	49.78	48.38	47.15	46.05	45.06	44.10	43.26
ρ/(g/cm^3)	3.36	3.54	3.69	3.83	3.95	4.06	4.17	4.27	4.36	4.46	4.54
V_{SiO_6}/Å^3	8.14	7.85	7.60	7.39	7.21	7.04	6.90	6.77	6.66	6.54	6.42
V_{MgO_6}/Å^3	12.26	11.46	10.86	10.38	9.97	9.63	9.34	9.07	8.84	8.63	8.44
O…O/Å	2.41	2.39	2.37	2.36	2.34	2.33	2.32	2.31	2.30	2.29	2.28
O–H/Å	1.20	1.19	1.19	1.18	1.17	1.17	1.16	1.15	1.15	1.14	1.14

Table A2. Structure parameters for Pm structure under pressure.

P/GPa	0	10	20	25	30	35	40	50	60	70	80	90	100
a/Å	4.81	4.71	4.64	4.61	4.59	4.56	4.54	4.50	4.46	4.43	4.40	4.38	4.35
B/Å	4.35	4.25	4.17	4.13	4.11	4.09	4.07	4.03	4.00	3.97	3.95	3.92	3.90
C/Å	2.86	2.81	2.77	2.75	2.73	2.71	2.70	2.67	2.64	2.62	2.59	2.57	2.55
β/(°)	93.35	92.52	92.01	91.82	91.66	91.52	91.40	91.19	91.01	90.86	90.72	90.61	90.50
V/Å3	59.84	56.15	53.45	52.30	51.38	50.55	49.78	48.38	47.15	46.05	45.06	44.15	43.32
ρ/(g/cm^{-3})	3.29	3.50	3.68	3.76	3.83	3.89	3.95	4.06	4.17	4.27	4.36	4.45	4.54
V_{SiO_6}/Å^3	8.21	7.87	7.61	7.49	7.39	7.30	7.21	7.04	6.90	6.77	6.65	6.54	6.43
V_{MgO_6}/Å^3	12.38	11.49	10.87	10.61	10.38	10.17	9.97	9.63	9.34	9.07	8.84	8.63	8.44
O…O_1	2.59	2.48	2.41	2.39	2.38	2.37	2.36	2.34	2.33	2.32	2.31	2.30	2.29
O–H_1	1.04	1.07	1.11	1.17	1.19	1.19	1.18	1.17	1.17	1.16	1.15	1.15	1.14
O…H_1	1.55	1.41	1.30	1.22	1.18	1.18	1.18	1.17	1.17	1.16	1.15	1.15	1.14
∠O–H_1	178.06	178.72	179.35	179.77	179.90	179.95	179.99	179.99	179.99	179.99	179.99	180.00	180.00
O…O_2	2.52	2.45	2.39	2.37	2.36	2.35	2.34	2.33	2.32	2.31	2.30	2.29	2.28
O–H_2	1.04	1.06	1.10	1.15	1.17	1.17	1.17	1.16	1.16	1.15	1.15	1.14	1.14
O…H_2	1.49	1.39	1.30	1.22	1.19	1.18	1.17	1.17	1.16	1.15	1.15	1.14	1.14
∠O–H_2	175.67	177.09	178.36	179.40	179.84	179.87	179.97	179.98	179.98	179.99	179.99	180.00	180.00

Table A3. Elastic constants of phase H (Pm (upper) and $P2/m$ (lower) symmetries) under pressure from 0 GPa to 100 GPa.

Pressure/GPa	C_{11}/GPa	C_{22}/GPa	C_{33}/GPa	C_{44}/GPa	C_{55}/GPa	C_{66}/GPa	C_{12}/GPa	C_{13}/GPa	C_{15}/GPa	C_{23}/GPa	C_{25}/GPa	C_{35}/GPa	C_{46}/GPa
0	367.2	424.5	384.6	113.1	110.6	164.4	91.9	82.6	19.8	115.0	–0.1	0.0	3.7
10	436.6	481.8	452.1	130.2	122.7	203.3	129.8	99.7	25.1	149.4	–0.1	0.1	–1.5
20	501.0	536.2	513.6	143.3	133.0	237.4	167.3	118.6	29.2	182.5	0.1	0.0	–5.8
30	560.5	586.8	570.4	154.7	142.2	267.2	203.5	138.7	33.1	214.9	0.0	0.0	–9.8
40	616.1	634.1	623.9	162.2	149.1	294.5	238.1	159.0	36.8	246.3	–0.2	0.2	–13.4
50	669.6	680.5	674.8	169.1	156.1	319.8	272.9	180.4	40.7	277.8	0.0	0.0	–16.8
60	721.5	725.7	723.4	172.9	162.2	343.9	307.3	202.3	44.6	308.6	0.2	–0.1	–19.7
70	771.5	770.0	770.5	176.4	167.8	367.0	341.0	224.6	48.1	339.0	–0.3	0.0	-22.5
80	820.0	813.6	816.1	181.3	172.7	388.6	374.7	246.6	50.7	368.8	–0.2	0.0	–25.4
90	868.5	855.5	860.2	183.2	176.5	409.7	407.9	269.2	54.1	398.5	–0.1	–0.1	–27.6
100	913.7	897.4	902.3	187.8	180.5	429.5	440.7	291.8	56.3	428.1	0.0	0.0	–30.4
0	364.4	288.2	286.0	134.4	100.5	100.3	79.3	74.8	0.0	69.8	0.0	20.7	25.7
10	435.3	376.2	362.0	181.1	122.7	117.6	94.6	108.6	0.0	111.5	-0.1	25.1	27.9
20	499.7	451.6	421.3	219.3	138.3	130.7	112.5	142.1	0.0	149.3	0.0	29.8	30.8
25	533.4	510.8	466.3	238.4	146.6	136.4	127.7	168.2	0.0	181.5	0.0	31.9	31.7
30	570.0	560.7	582.3	265.5	151.0	140.5	139.5	214.1	–0.1	203.7	–0.1	33.9	44.0
35	598.0	588.1	609.0	279.8	155.4	144.6	149.2	230.8	0.1	221.6	–0.1	36.0	45.6
40	623.5	617.1	632.6	293.7	160.2	149.5	159.3	246.2	0.0	240.3	0.0	36.9	46.3
50	674.7	670.5	679.6	320.2	167.2	156.6	180.8	277.2	–0.1	274.9	0.3	40.0	47.2
60	723.4	721.9	724.5	344.2	172.5	162.5	202.5	307.9	0.1	308.7	–0.1	43.8	48.4
70	770.2	772.1	768.7	367.0	178.3	167.9	224.6	338.4	–0.1	342.9	0.2	47.0	49.4
80	815.8	820.9	811.8	388.7	179.7	173.3	246.3	368.2	0.0	376.4	0.0	49.9	50.7
90	859.2	868.5	855.4	409.4	184.1	177.5	268.9	398.1	0.0	409.7	–0.1	52.9	51.2
100	902.0	914.7	896.1	429.4	187.3	182.7	291.3	427.5	0.0	442.4	0.1	54.9	52.7

Table A4. Raman-active frequency and intensity of $P2/m$ structure as a function of pressure.

Pressure/GPa	0	10	20	30	40	50	60	70	80	90	100
Frequencyc/cm^{-1}	349.4818	382.4308	410.9709	435.3306	457.015	476.6924	493.0361	509.4873	523.9831	537.4606	549.5454
Intensity/Å^4	0.800234	0.77685	0.733266	0.692626	0.652239	0.582296	0.52771	0.43215	0.300715	0.180913	0.098367
Frequency/cm^{-1}	412.9844	432.3021	450.4995	466.9492	481.5953	495.5504	508.9915	521.9069	534.2343	547.336	560.6787
Intensity/Å^4	0.157657	0.171733	0.178912	0.194593	0.219295	0.262507	0.309598	0.37532	0.485055	0.591459	0.645387
Frequency/cm^{-1}	498.5078	537.1112	571.4585	598.5855	621.7804	642.9057	663.1307	681.1618	698.2647	712.6056	725.7728
Intensity/Å^4	6.429158	7.242249	5.993983	6.444333	6.150669	6.838134	6.602587	6.739157	7.341615	7.65039	7.142227
Frequency/cm^{-1}	609.8225	641.4085	670.4834	695.8782	718.2639	739.2223	759.1753	778.5713	797.9474	816.3265	834.1065
Intensity/Å^4	6.380345	6.569545	5.976761	5.148973	4.531606	4.077391	3.707996	3.183591	2.374422	2.113025	1.734624
Frequency/cm^{-1}	726.42	758.7131	787.0997	812.4541	835.0735	855.9453	875.47	893.6755	910.1731	926.3712	941.7335
Intensity/Å^4	5.478971	5.405128	4.935785	4.430534	4.284994	4.271514	3.7518	3.58728	3.457626	3.494085	3.36311
Frequency/cm^{-1}	812.8016	841.0087	867.5941	892.6684	916.2712	938.7393	960.1933	981.1215	1001.404	1020.982	1040.027
Intensity/Å^4	4.390647	4.191848	3.828857	3.537355	3.325726	2.978218	2.908961	3.104527	2.828503	2.582652	2.732853

Table A5. Raman frequency for phase H with *Pm* symmetry. Note: vacancies means no Raman-active vibrational modes exist.

Pressure/GPa	0	10	20	25	30	35	40	50	60	70	80	90	100
	226.16	275.45	257.43	92.40									
	264.96	307.19	290.27	125.39									
	288.13	327.39											
	297.97	328.05	378.33										
	349.44	361.85	384.95	418.83	435.07	446.34	457.05	476.69	493.04	509.51	524.04	537.50	549.58
	386.85	418.98	445.07	458.28	466.69	474.23	481.67	495.55	509.02	521.96	534.29	547.38	560.71
	450.49	474.20	477.51	465.89									
	460.43	487.48	490.17										
	472.49	511.44	551.53	578.11	597.60	610.35	621.76	642.93	663.14	681.18	698.21	712.58	725.78
	519.30	545.72											
Frequency/cm^{-1}	556.05	588.09	603.25	600.00									
	567.98	598.56	645.31	680.00	695.61	707.15	718.22	739.22	759.23	778.64	797.97	816.36	834.15
	638.98	696.66	756.72	784.88									
	660.74	726.54	778.83	798.27	812.22	824.01	835.03	855.94	875.48	893.68	910.15	926.36	941.74
	780.21	805.24	834.83	870.97	891.94	904.36	916.24	938.71	960.17	981.11	1001.36	1020.95	1040.01
	1008.87	1101.94											
	1266.41	1336.30	1343.68	1220.15	1235.91								
	1292.12	1349.39	1394.42	1350.14	1342.87	1379.50							
	1443.26	1517.99	1528.74										
	2452.29	2032.61	1618.44	1555.10									
	2479.66	2125.39	1807.93	1703.47	1708.76								

Table A6. Raman intensity for phase H with Pm symmetry.

Pressure/GPa	0	10	20	25	30	35	40	50	60	70	80	90	100
	0.22	0.05	4.05	0.64									
	0.74	3.72	2.74	1.16									
	0.15	0.38											
	3.37	1.72	0.06										
	0.84	0.76	0.54	0.67	0.70	0.67	0.66	0.59	0.55	0.43	0.30	0.17	0.11
	0.14	0.16	0.18	0.18	0.19	0.20	0.22	0.26	0.31	0.37	0.48	0.59	0.64
	0.43	0.25	1.53	0.16									
	0.85	2.48	0.15										
	4.22	2.55	2.30	3.16	5.80	6.20	6.44	7.09	6.67	6.83	6.56	7.29	6.67
	0.16	0.10											
Intensity/Å^4	1.02	4.51	4.64	2.93									
	8.72	3.49	3.00	5.01	5.05	4.86	4.46	3.78	3.70	2.73	2.37	2.00	1.66
	4.11	3.80	4.37	1.11									
	3.10	1.54	0.79	3.66	4.40	4.30	4.24	3.86	4.22	3.86	3.88	3.50	3.26
	10.96	9.23	6.02	3.44	3.49	3.44	3.33	3.13	2.96	3.08	3.20	2.92	2.83
	0.30	0.14											
	1.30	0.60	17.55	3.26	0.14								
	8.78	10.12	0.19	7.07	0.72	0.21							
	1.71	3.30	17.41										
	274.77	151.63	31.29	1.12									
	392.40	195.11	54.16	3.06	0.17								

References

[1] Huang X, Xu Y and Karato S 2005 *Nature* **434** 746
[2] Faccenda M, Burlini L, Gerya T V and Mainprice D 2008 *Nature* **455** 1097
[3] Komabayashi T, Omori S and Maruyama S 2005 *Phys. Earth Planet. Int.* **153** 191
[4] Akimoto S and Akaogi M 1980 *Phys. Earth Planet. Int.* **23** 268
[5] Ohtani E, Toma M, Litasov K, Kubo T and Suzuki A 2001 *Phys. Earth Planet. Int.* **124** 105
[6] Ghosh S and Schmidt M W 2014 *Geochim. Cosmochim. Acta* **145** 72
[7] Sclar C B, Carrison L C and Schwartz C M 1965 *Trans. Am. Geophys. Union* **46** 184
[8] Ohtani E, Mizobata H and Yurimoto H 2000 *Phys. Chem. Miner.* **27** 533
[9] Komabayashi T, Omori S and Maruyama S 2004 *J. Geophys. Res.: Solid Earth* **109** B03206
[10] Melekhova E, Schmidt M W, Ulmer P and Pettke T 2007 *Geochim. Cosmochim. Acta* **71** 3348
[11] Liu L 1987 *Phys. Earth Planet. Int.* **49** 142
[12] Frost D J and Fei Y 1998 *J. Geophys. Res.: Solid Earth* **103** 7463
[13] Shieh S R, Mao H, Hemley R J and Li C M 1998 *Earth Planet. Sci. Lett.* **159** 13
[14] Tsuchiya J 2013 *Geophys. Res. Lett.* **40** 4570
[15] Bindi L, Nishi M, Tsuchiya J and Irifune T 2014 *Am. Mineral.* **99** 1802
[16] Nishi M, Irifune T, Tsuchiya J, Tange Y, Nishihara Y, Fujino K and Higo Y 2014 *Nat. Geosci.* **7** 224
[17] Tsuchiya J and Mookherjee M 2015 *Sci. Rep.* **5** 15534
[18] Refson K, Tulip P R and Clark S J 2006 *Phys. Rev. B* **73** 155114
[19] Hohenberg P and Kohn W 1964 *Phys. Rev.* **136** B864
[20] Kohn W and Sham L J 1965 *Phys. Rev.* **140** A1133
[21] Clark S J, Segall M D, Pickard C J, Hasnip P J, Probert M J, Refson K and Payne M C 2005 *Kristallogr.* **220** 567
[22] Perdew J P and Wang Y 1992 *Phys. Rev. B* **45** 13244
[23] Hamann D R 1997 *Phys. Rev. B* **55** R10157
[24] Umemoto K, Wentzcovitch R M, Baroni S and De G S 2004 *Phys. Rev. Lett.* **92** 105502
[25] Troullier N and Martins J L 1991 *Phys. Rev. B* **43** 1993
[26] Monkhorst H J and Pack J D 1976 *Phys. Rev. B* **13** 5188
[27] Pfrommer B G, Cote M, Louie S G and Cohen M L 1997 *J. Comput. Phys.* **131** 233
[28] Karki B B, Stixrude L and Wentzcovitch R M 2001 *Rev. Geophys.* **39** 507
[29] Baroni S, De G S, Dal C A and Giannozzi P 2001 *Rev. Mod. Phys.* **73** 515
[30] Gonze X 1997 *Phys. Rev. B* **55** 10337
[31] Porezag D and Pederson M R 1996 *Phys. Rev. B* **54** 7830
[32] Refson K, Tulip P R and Clark S J 2006 *Phys. Rev. B* **136** 864
[33] Holzapfel W B 1972 *J. Chem. Phys.* **56** 712
[34] Pruzan P, Chervin J C, Wolanin E, Canny B, Gauthier M and Hanfland M 2003 *J. Raman Spectrosc.* **34** 591
[35] Tsuchiya J, Tsuchiya T and Tsuneyuki S 2005 *Am. Mineral.* **90** 44
[36] Sano-Furukawa A, Komatsu K, Vanpeteghem C B and Ohtani E 2008 *Am. Mineral.* **93** 1558
[37] Murnaghan F D 1944 *Proc. Natl. Acad. Sci.* **30** 244
[38] Goncharov A F, Struzhkin V V, Somayazulu M S, Hemley R J and Mao H K 1996 *Science* **273** 218
[39] Ohira I, Ohtani E, Sakai T, Miyahara M, Hirao N, Ohishi Y and Nishijima M 2014 *Earth Planet. Sci. Lett.* **401** 12
[40] Wen L and Helmberger D V 1998 *Science* **279** 1701
[41] Richards M A, Duncan R A and Courtillot V E 1989 *Science* **246** 103
[42] Musgrave M J P 1970 *Crystal Acoustics* (San Fransisco: Holden-Day)
[43] Walker A M and Wookey J 2012 *Comput. Geosci.* **49** 81
[44] Fateley W G, McDevitt N T and Dollish F R 1971 *Appl. Spectrosc.* **25** 155
[45] Delattre S, Balan E, Lazzeri M, Blanchard M, Guillaumet M, Beyssac O, Haussuhl E, Winkler B, Salje E K H and Calas G 2012 *Phys. Chem. Miner.* **39** 93
[46] Huang X L, Li F F, Huang Y P, Wu G, Li X, Zhou Q, Liu B B and Cui T 2016 *Chin. Phys. B* **25** 037401
[47] Umemoto K and Wentzcovitch R M 2005 *Phys. Rev. B* **71** 012102
[48] Hemley R J, Jephcoat A P, Mao H K, Zha C S, Finger L W and Cox D E 1987 *Nature* **330** 737
[49] Mainprice D, Page Y L, Rodgers J and Jouanna P 2007 *Earth Planet. Sci. Lett.* **259** 283
[50] Tsuchiya J and Tsuchiya T 2009 *Phys. Earth Planet. Int.* **174** 122